International Journal of Concrete Structures and Materials

RESEARCH Open Access

Cracking Behavior of Ceramsite Aerated Concrete Block Infill Wall in the Coastal Areas

Ruige Li[1*], Huadong Cui[2*], Lingchao Ding[3], Haiping Ni[3], Shangquan Xu[4] and Huiling Wu[5]

Abstract

Ceramsite aerated concrete blocks (CACB) are widely used in reinforced concrete frame infill walls due to their green, energy-saving, waste utilization, and thermal insulation characteristics. Investigations into building projects in areas with low seismic intensity and frequent typhoons have found that the cracking of CACB infill walls is severe, which hinders the use of this material. This article was dedicated to studying the reasons and development process of cracks in CACB infill walls, and proposing solutions. First, a 13 story framework building was analyzed using PKPM software to study the inter-story drift ratio under local reference wind pressure and gust wind pressure. Then, three full-scale models were made for quasi-static tests under horizontal loads to study the correlation between inter-story drift ratio and infill wall cracking. Experimental studies have shown that the inter-story drift ratio was 1/2149 and 1/2347 for infill wall frames with and without windows, respectively, when CACB infill walls cracked. Comparing PKPM analysis and experimental results, it could be seen that when the building was subjected to local reference wind pressure, the inter-story drift ratio was 1/2433, which was smaller than the cracking inter-story drift ratio. When subjected to the wind pressure corresponding to the gust wind, the structural deformation was much greater than the cracking inter-story drift ratio. Therefore, it could be concluded that the main reason for diagonal cracks in CACB infill walls was the unreasonable use of reference wind pressure in current design. To avoid the diagonal cracks, gust wind pressure should be used as the horizontal load instead of reference wind pressure in design. Simultaneously to improve both structural construction measures and material crack resistance to avoid cracking of CACB infill walls.

Keywords Ceramsite aerated concrete block (CACB), Infill wall, Horizontal load, Wind load, Cracks, Inter-story drift

1 Introduction

Ceramsite aerated concrete is regarded as green building material in structural engineering, owing to its eco-friendliness, energy efficiency, waste management capabilities, and insulation properties (Bernhardt et al., 2014; Cheng et al., 2018; Fan et al., 2021; Li et al., 2023a, 2023b). In the southeast coastal region of Zhejiang Province, China, the foundation predominantly comprises thick mucky silty clay (Lu et al., 2021; Xu et al., 2022c). Lots of it is dug up every year as construction waste. These wastes can be used as the main raw materials for sintering ceramsite (He et al., 2015; Hong et al., 2013; Ma et al., 2021a). Ceramsite concrete is composed of ceramsite instead of coarse aggregate (Chen et al., 2020; Li et al., 2021; Xu et al., 2022b). The application of ceramsite concrete can effectively utilize construction

Journal information: ISSN 1976-0485 / eISSN 2234-1315.

*Correspondence:
Ruige Li
lrg@tzc.edu.cn
Huadong Cui
cuihd9999@163.com
[1] School of Civil Engineering and Architecture, Taizhou University, Jiaojiang, Taizhou 318000, China
[2] Taizhou Construction Quality and Safety Service Center, Taizhou 318000, China
[3] Taizhou Yuanxin Construction Engineering Co., Ltd, Taizhou 318000, China
[4] Taizhou Urban and Rural Planning and Design Institute Co., Ltd, Jiaojiang, Taizhou 318000, China
[5] Taizhou Haoqiang Building Materials Co., Ltd, Jiaojiang, Taizhou 318000, China

Springer Open

© The Author(s) 2025. **Open Access** This article is licensed under a Creative Commons Attribution-NonCommercial-NoDerivatives 4.0 International License, which permits any non-commercial use, sharing, distribution and reproduction in any medium or format, as long as you give appropriate credit to the original author(s) and the source, provide a link to the Creative Commons licence, and indicate if you modified the licensed material. You do not have permission under this licence to share adapted material derived from this article or parts of it. The images or other third party material in this article are included in the article's Creative Commons licence, unless indicated otherwise in a credit line to the material. If material is not included in the article's Creative Commons licence and your intended use is not permitted by statutory regulation or exceeds the permitted use, you will need to obtain permission directly from the copyright holder. To view a copy of this licence, visit http://creativecommons.org/licenses/by-nc-nd/4.0/.

waste and reduce environmental pollution (Wang et al., 2022; Shang et al., 2022; Xu et al., 2022a; Liu et al., 2012) Ceramic aerated concrete block (CACB) was a lightweight and thermally insulating wall material that was commonly employed in construction engineering (Ma et al., 2021b, 2021c; Zhang et al., 2020). However, numerous cracks have been observed in CACB infill walls of buildings, thereby hindering its extensive use in southeast coast of Zhejiang Province, China (Zhang et al., 2024; Liu et al., 2024). From June 2018 to August 2021, more than 50 buildings in Taizhou and adjacent urban areas of Zhejiang province were investigated for external CACB infill wall cracks. The study revealed that the CACB walls exhibited numerous inclined cracks, which often traversed the entire thickness of the wall and appeared mostly at the bottom and middle floors of the building, with fewer occurrences at the top. These cracks typically manifested during the final stages of construction or within 1–2 years following completion.

The mechanical and physical properties of CACB are different from those of ordinary concrete block (Li et al., 2023a, 2023b; Tan et al., 2018; Zhai et al., 2017). CACB not only has the advantages of light weight and good heat insulation, but also has the drawbacks of low strength (Guo et al., 2011; Li et al., 2022). In structural designs, infill walls, as unstructured components, are usually not considered for their contribution to the overall strength of the building, but only act as a constant load on the structure (Pankaj et al., 2005). In fact, research has shown that if there are infill walls, the overall stress performance of the frame structure is significantly different compared to when there are no infill walls (Jonathan et al., 2024; Arton et al., 2018; Ning et al., 2019). In addition, different materials of filling wall contribute differently to the stiffness and seismic resistance of buildings (Wijaya et al., 2020; Niu et al., 2024). The interaction between infill walls and structures can alter the seismic response of structures and consequently affect the destructive characteristics (Lu et al., 2024). Whether there are windows in the infill wall has a significant different impact on the mechanical performance of the frame structure too (Laura et al., 2020). The reports on the mechanical properties and vulnerability of CACB as infill wall are very limited, leading to the lack of evidence for its applicability in engineering and also lack of solutions to the widespread engineering quality problems of CACB infill walls.

In the southeast coast of China, typhoon makes landfall frequently and causes much damage on buildings and other properties (Huang et al., 2020, 2024). The southeast coast of China experiences more than three typhoons each year in average from 1951 to 2022, during which a total of 243 typhoons was recorded. The maximum wind speed near the center of Typhoon Lekima in August 2019 was over 60 m/s (*Typhoon Webpage in National Meteorological Centre of China*, 2023), which corresponded to a wind pressure of about 2.34 kN/m^2. In the city, the wind load has a great influence on tall and multi-story buildings (Gu et al., 2023). The impact of extreme typhoon loads on a multi-story frame structure can result in significant inter-story drift, which is an important performance index in the wind-resistant building design. Typhoons and torrential rains frequently land, then the cracks of the external CACB infill wall are easy to cause rainwater leakage, which seriously affects the serviceability and normal functions of buildings. It caused many engineering disputes between developers and users.

To explore whether the severe cracking of CACB filled walls in the southeastern coastal areas of China was related to the frequent typhoons in this region, a PKPM calculation and analysis was performed on a 13-story residential structure. Horizontal seismic loads, horizontal loads of the reference wind speed, and horizontal loads of the gust wind speed provided by the local meteorological department were applied on the model, respectively. The inter-story drift ratio of the house under various horizontal loads was calculated by PKPM building structural analysis software. At the same time, three frame models were made for quasi-static tests. Data such as lateral displacement, crack development, and crack distribution of the test model under the action of horizontal forces were collected. The PKPM calculation results were compared with the model test results to analyze the causes of wall cracking and propose solutions.

2 Calculation and analysis of building

2.1 Model overview

The project was a 13 story frame structure residential building located in Taizhou, Zhejiang Province, China (Li et al., 2024a). The standard floor structure layout plan is shown in Fig. 1. The C40 concrete was used for columns on the first and the 2nd floor, C30 concrete was used for columns on the 5th floor and above, and C35 concrete was used for columns on other floors. The main cross-sectional dimensions of the column were 800 mm × 850 mm and 600 mm × 650 mm. The concrete strength grade of beams and slabs was the same as that of columns, and the cross-sectional dimensions of horizontal and vertical frame beams were 300 mm × 700 mm. The finite element model of the structure is shown in Fig. 2.

The dead load was the self-weight of the structure, and the vertical live load was analyzed based on the residential floor value of 2.0 kN/m^2, and the live load on the roof was 2.0 kN/m^2 according to the *load code for the design of building structures (GB 50009–2012)*. The horizontal load was input in the four cases. Case 1: the horizontal load was the seismic fortification intensity of 6 degrees

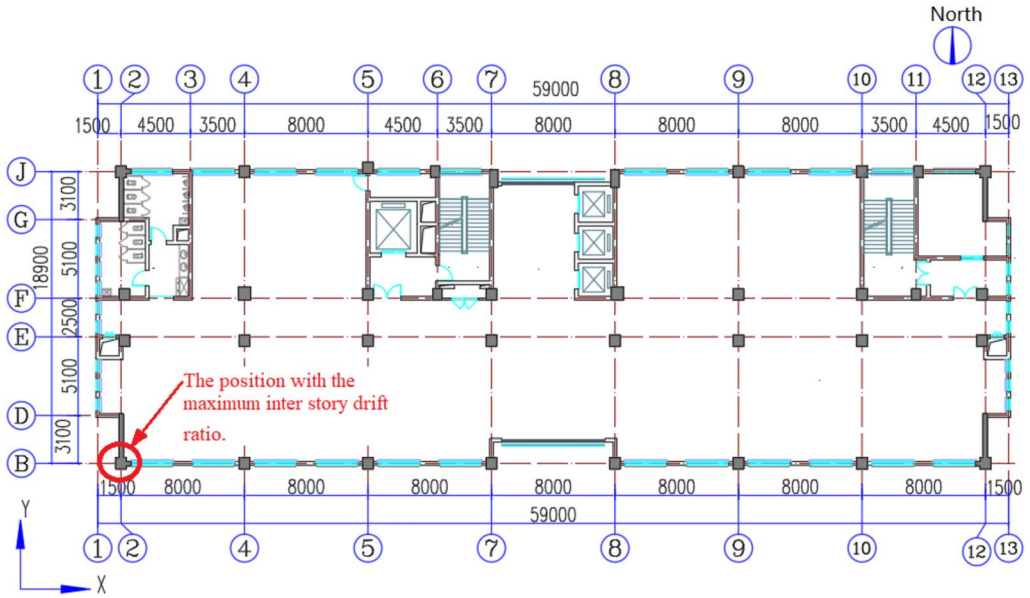

Fig. 1 Layout plan of standard floor (unit: mm)

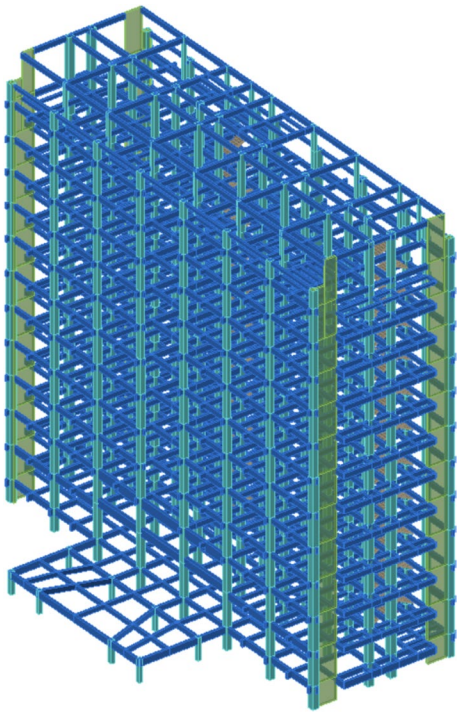

Fig. 2 Finite-element model of structure

(considering accidental eccentricity). Case 2: the horizontal load was the local reference wind pressure of 0.7 kN/m^2. Case 3: the horizontal load wind pressure value was 1.0 kN/m^2. Case 4: the horizontal load wind pressure value was 1.27 kN/m^2.

2.2 PKPM calculation principle

PKPM structural analysis software was used to analyze the inter-story drift of the 13 story frame structure residential building. PKPM is a series of building engineering design software primarily used for structural analysis and design based on the finite element method (FEM) (Wang et al., 2013). The basic principle is to discretize the structure into a finite number of elements, which are interconnected by nodes. For this frame structure, beams, columns, and walls are decomposed into different elements. Each element has its own stiffness matrix, which describes the deformation characteristics of the element under loads (Wang et al., 2016). During the calculation process, the first step is to establish a structural calculation model by inputting the geometric information, material properties, and load information. The software then calculates the stiffness matrix for each element and assembles these individual element stiffness matrices to form the overall stiffness matrix for the entire structure (Li et al., 2015). When a load is applied to the structure, the equilibrium equations are established based on the principles of force balance and deformation compatibility. The software solves this system of equations to obtain the nodal displacements. Once the nodal displacements are obtained, the internal forces (including axial forces, shear forces, bending moments, etc.) for each element can be calculated based on the material's constitutive relationship. These internal forces are serving as the basis for determining whether the structural components meet the requirements for strength, stability, and deformation (Ou et al., 2012).

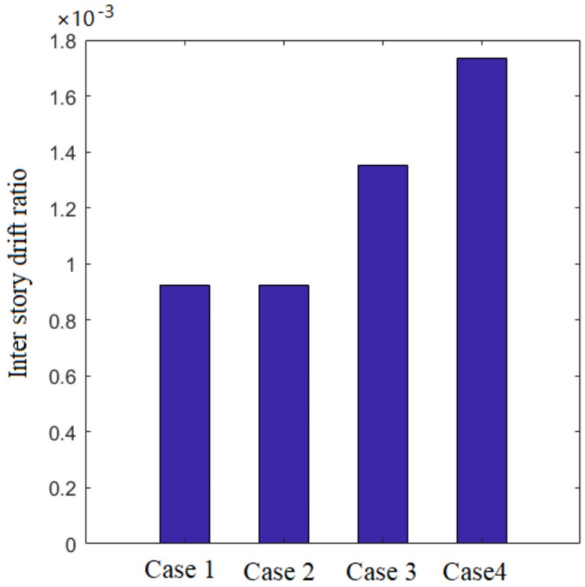

Fig. 3 Maximum inter-story drift ratio of the structure

2.3 Calculation results

In the four cases horizontal load, the maximum inter-story drift ratio of the structure appeared at the intersection of the *B*-axis and the 2-axis on the 6th floor (marked in Fig. 1 by red circle and red words). As shown in Fig. 3, the maximum inter-story drift ratio θ in case 1, 2, 3, and 4 was 1/1081 (0.9251×10^{-3}), 1/1082 (0.925×10^{-3}), 1/739 (1.353×10^{-3}) and 1/577 (1.733×10^{-3}), respectively.

Table 1 Mechanical properties of steel bars

Type of steel bar	Diameter of rebar *d* (mm)	Yield strength f_{yk} (N/mm^2)	Ultimate strength f_{uk} (N/mm^2)	Young's modulus E_s ($\times10^5$N/mm^2)
HPB300	6	304.1	436.5	2.09
HRB400	20	411.2	568.5	2.03

3 Model test

3.1 Test model design and materials

The test specimen was designed to adhere to the principle of strong column and weak beam while also meeting the necessary structural requirements. The dimensions and reinforcement of the specimen can be seen in Figs. 4 and 5. The longitudinal reinforced bars for both the beam and column have a strength grade of HRB400, while

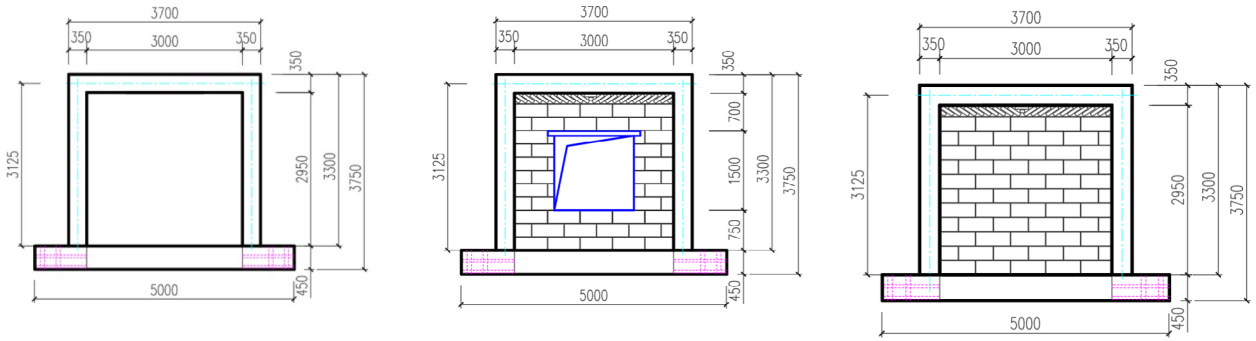

(a) Test model F0 (b) Test model F1 (c) Test model F2

Fig. 4 Design of three test models (unit: mm)

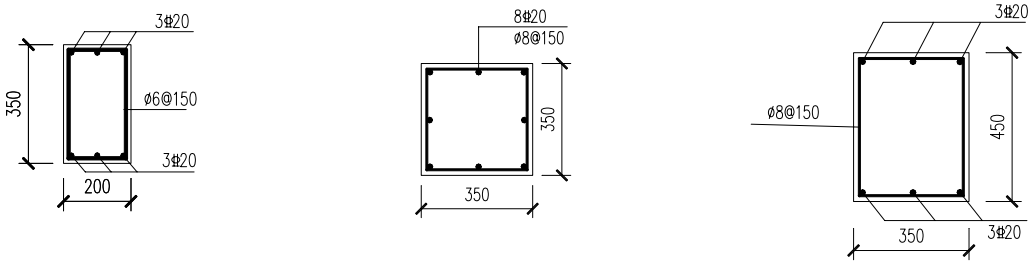

(a) Top beam (b) Column (c) Bottom beam

Fig. 5 Section diagram of the test model elements (unit: mm

Table 2 Mix proportions of concrete and the mechanical properties

Mix proportions of concrete				Mechanical properties of concrete		
Mass per unit volume (kg/m^3)						
Cement	Water	Sand	Coarse aggregate	Compressive strength $f_{cu,m}$ (N/mm^2)	Tensile strength $f_{t,m}$ (N/mm^2)	Young's modulus E_c ($\times 10^4$N/mm^2)
487	185	533	1245	43.3	3.16	3.28

Fig. 6 Photo of CACB

the stirrups have a strength grade of HPB300 and were deployed throughout the entire length of the beam and column. Mechanical properties of steel bars are listed in Table 1. The frame concrete has a design strength grade of C40, the mix proportions of concrete and the mechanical properties are given in Table 2. The frame column has a design axial compression ratio of $n=0.3$ with an axial pressure of 702 kN.

The infill walls were constructed using special masonry mortar and CACB with dimensions of 200 mm×240 mm×600 mm which were made in a local factory in Taizhou, Zhejiang province (Fig. 6). The mix proportions of CACB are shown in Table 3 and the mechanical properties are shown in Table 4. To ensure stability, five rows of tie bars were added based on the number of layers of blocks, with the first, third, and fifth layers having a tie bar length of 900 mm and the second and fourth layers having a length of 700 mm.

The top of the infill wall was brick masonry. This brick was a non-sintered lime sand brick cured by steam pressure, with dimensions of 240 mm×120 mm×60 mm. The bricks were built diagonally above the CACB. The upper surface of the bricks was closely contact to the beam, and its left and right sides were contact to the columns. Its function was that when the upper beam undergoes flexural deformation under vertical load, the inclined bricks could change the inclination angle, thereby avoiding the filling wall from being subjected to vertical pressure from the beam.

3.2 Loading mechanism and strain gauge arrangement

The test setup and loading device is shown in Fig. 7. Initially, a vertical load of 702 kN was applied to each column, divided into four levels. The loading speed of vertical load was 20 kN/min. Once the vertical load reaches the target value, it was maintained at a constant level, and a horizontal load was then applied. When the horizontal load was less than 40 kN, monotonic loading applied by speed of 16 kN/min. After exceeding 40 kN, the load increased by 10 kN for each stage until it reaches 120 kN, after which it increased by 20 kN until it reached 220 kN. Thereafter, it increased by 30 kN until it reached 280 kN. In addition, one loop load was applied on the structures for each level. The speed of applying the load was 10 min for a loop. The loading protocol is shown in Fig. 8.

The horizontal displacement D_1 was measured by a displacement meter fixed to an independent steel frame at one end of the beam. The other displacement meter was set in the horizontal direction of the ground beam to measure the horizontal movement of the ground beam D_2. Two displacement meters were set in the vertical direction of the two sides of the ground beam to measure the possible warping displacement D_3 and D_4. The setup of the displacement meters and strain gauge are shown in Fig. 9. The inter-story drift ratio θ was calculated according to Eq. (1) as

$$\theta = D_1 - D_2 + \frac{D_3 - D_4}{L}H \tag{1}$$

Table 3 Mix proportions of CACB

Mass per unit volume (kg/m^3)						
Cement	Fly ash	High strength ceramsite	Ceramsite sand	Water reducer	Foaming agent	Water
300	250	270	110	0.45	0.83	180

Table 4 Mechanical properties of CACB

Compressive strength $f_{cuA,m}$ (N/mm^2)	Tensile strength $f_{tA,m}$ (N/mm^2)	Young's modulus E_{cA} ($\times 10^3$N/mm^2)
5.035	0.605	4.83

where L was the distance between the displacement meter D_3 and D_4, and H was the distance from the top beam axis to the upper edge of the ground beam.

3.3 Model test results

The experimental data obtained under varying horizontal loads are presented in Table 5.

3.3.1 Component to model F0

When a horizontal load of 80 kN was applied, the first inclined cracks appeared at the right end of the beam. These cracks were inclined down at an angle of about 60° along the direction of loading (thrust to the left). The width of the cracks was measured to be 0.20 mm, and there was no apparent crack at the left end of the beam. The maximum inter-story drift ratio was calculated to be $\theta = 0.786 \times 10^{-3}$(the expression of fractions is: $\theta = 1/1272$). The initial fracture distribution is illustrated in Fig. 10a by red line.

As the horizontal force increased, the number and width of cracks gradually increased. When the horizontal load reached 120 kN, a larger width crack appeared at the other end of the beam. The maximum width of the crack was 0.41 mm, and it was inclined downwards about 55°.

As the horizontal load was raised to 180 kN, a noticeable increase in the crack at the end of the beam was observed, with its maximum width measuring 0.55 mm. Cross oblique cracks were evidenced in the core area of beam–column joints. In addition, inclined cracks measuring approximately 60° in oblique direction appear in the upper and lower portions of the beam at 1/3 span from the end. The lower column foot also exhibits an oblique crack with a width of 0.1 to 0.4 mm and a horizontal angle of approximately 26°.

As the horizontal load increased to 200 kN, the crack at the end of the beam exhibits further progression, and the core area of the beam–column joints also displayed increased cracks, with a maximum width of 1.0 mm, as shown in Fig. 10b. The width and number of oblique cracks in the lower column base also continued to increase, with the maximum width measuring approximately 0.35 mm. The maximum width of the crack at the upper beam end was observed to be 0.55 mm. At 1/3 span from the end of the frame beam, the width and number of inclined cracks in the upper and lower parts of the beam section increased, with the maximum width reaching 0.40 mm.

As the horizontal load increased to 250 kN, the crack in the core area of the beam–column joints underwent a rapid increase, with the maximum width reaching 2.3 mm. Ultimately, the concrete at the bottom of the column base was crushed, resulting in the destruction of the specimen.

3.3.2 Component to model F1

Upon increasing the horizontal load to 60 kN (tensile force), the first small cracks appeared at the lower window corner of the infill wall, inclined at an angle

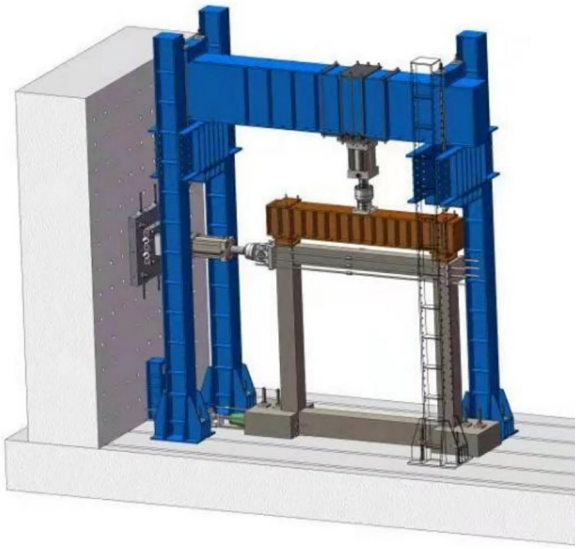

Fig. 7 Test setup

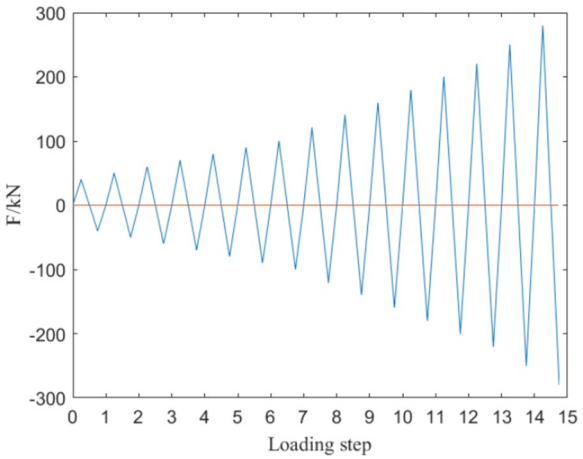

Fig. 8 Loading protocol

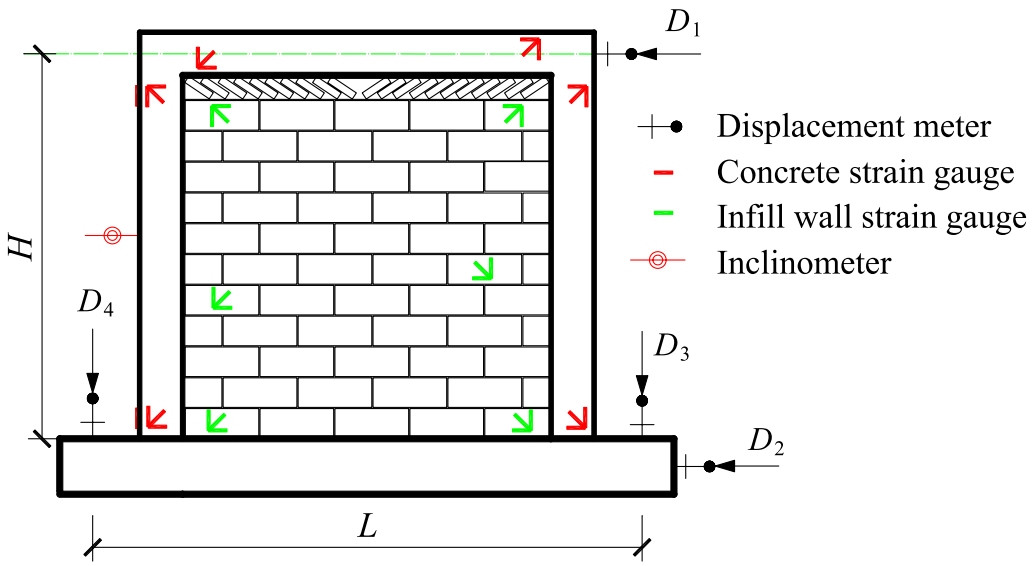

Fig. 9 Measuring point of displacement and strain gauge

of approximately 75° along the direction of the force. The maximum width of these cracks was measured at 0.22 mm. The maximum inter-story drift ratio was $\theta = 0.465 \times 10^{-3}$ (the expression of fractions is: $\theta = 1/2149$). The distribution of these cracks is shown in Fig. 11.

As the horizontal load was gradually increased from 60 to 80 kN, the number and width of cracks increased, as shown in Fig. 12 with blue lines. Similarly, when the load increased from 100 to 120 kN, the number and width of cracks on the infill wall also increased significantly. When the load was further increased to 140 kN, vertical cracks emerged on the upper right side of the beam. The distribution of these cracks is presented in Fig. 12 with green lines. Subsequently, as the horizontal load increased to 180 kN, the crack width widens considerably, with the maximum crack width reaching 0.95 mm. The distribution of these cracks is presented in Fig. 9 with yellow lines.

When subjected to a horizontal load at 250 kN, a significant increase in the number and width of cracks was observed. New inclined cracks appeared in the upper two corners of the window hole with a width of approximately 1.2 mm. During the loading process, the mortar exhibited signs of failure, producing an audible "click click" sound.

When the horizontal load increased to 280 kN, the width of the inclined crack in the upper two corners of the window hole increased to about 1.5 mm. Other existing cracks had also increased dramatically in width. There were also wider vertical cracks in the upper part of the beam. The cracking sound increased, and more mortar fell from the CACB wall. The distribution of these cracks from 200 to 280 kN is presented in Fig. 10 with pink lines. As depicted in the figure, the cracks were all distributed obliquely. The shape of the crack distribution in the upper part of the window hole was inverted V-shaped, and in the lower part of the window hole, it was V-shaped.

3.3.3 Component to model F2

When subjected to a horizontal tensile force of 90 kN, the CACB infilled wall developed its first round of small cracks in the middle of the wall, with a width 0.2–0.3 mm. The maximum inter-story drift ratio was $\theta = 0.426 \times 10^{-3}$ (the expression of fractions is: $\theta = 1/2347$). The cracks were inclined down about 60° along the direction of loading, which was towards the right. The distribution of cracks is illustrated in Fig. 13.

As the horizontal load increased from 90 to 140 kN, the number of cracks on the CACB infilled wall increased rapidly, and the crack width expanded too, as shown in Fig. 14 by green lines. When the horizontal load was further increased to 180 kN, the crack width increased significantly, with the maximum crack width reaching 0.68 mm. The crack distribution under a horizontal load of 180 kN is shown in Fig. 14 by yellow lines.

As the horizontal load was increased to 250 kN, there was a notable increase in both the number and width of new cracks, with an approximate width of 1 mm as evidenced in Fig. 14 with pink lines.

Upon a load of 280 kN, a discernible inclined crack appeared in the middle of the infilled wall, which propagated through previous cracks observed at loads of 90 kN, 140 kN, and 180 kN. This crack had a width

Table 5 Measured results of inter-story drift and lateral stiffness

Measurement indicators	The numeric value corresponding to the indicators													No. of Frame
Horizontal load/kN	40	60	80	90	100	120	140	160	180	200	220	250	280	
Inter-story drift in beam axis/mm	1.140	1.776	2.457	2.923	3.388	4.384	5.483	6.877	8.636	10.889	13.503	35.996	/	F0
	0.377	1.454	2.092	2.418	2.743	3.876	4.677	5.613	6.418	7.242	9.139	12.403	15.945	F1
	0.190	0.691	1.022	1.332	1.566	2.005	2.422	2.861	3.271	3.879	4.599	5.887	7.338	F2
$\theta/(\times 10^{-3})$	0.365	0.568	0.786	0.935	1.084	1.403	1.755	2.201	2.764	3.484	4.321	11.519	/	F0
	0.121	0.465	0.669	0.774	0.878	1.240	1.497	1.796	2.054	2.317	2.924	3.969	5.102	F1
	0.061	0.221	0.327	0.426	0.501	0.642	0.775	0.916	1.047	1.241	1.472	1.884	2.348	F2
Test value of lateral stiffness/($\times 10^4$N/mm)	3.509	3.378	3.256	3.080	2.952	2.737	2.553	2.327	2.084	1.837	1.629	0.695	/	F0
	10.610	4.127	3.824	3.723	3.646	3.096	2.993	2.851	2.805	2.762	2.407	2.016	1.756	F1
	21.053	8.683	7.828	6.757	6.386	5.985	5.780	5.592	5.503	5.156	4.784	4.247	3.816	F2
Lateral stiffness ratio (test value/theoretical value)	1.000	0.963	0.928	1.044	0.841	0.780	0.728	0.663	0.594	0.523	0.464	0.198	/	F0
	3.024	1.176	1.090	1.262	1.039	0.882	0.853	0.812	0.799	0.787	0.686	0.574	0.500	F1
	6.000	2.475	2.231	2.290	1.820	1.706	1.647	1.594	1.568	1.469	1.363	1.210	1.087	F2

(a) Distribution of the initial cracks

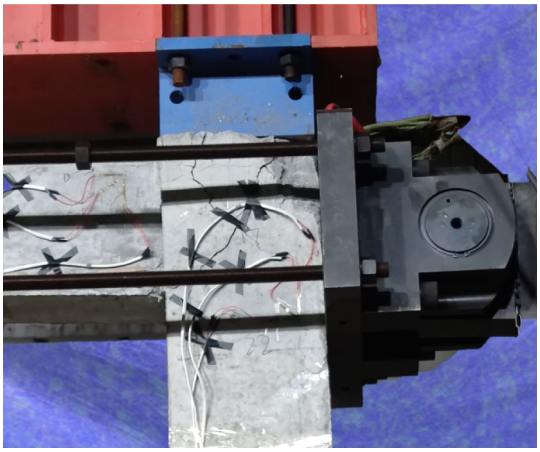

(b) The cracks distribution at 200 kN

Fig. 10 Distribution of the cracks in model F0

Fig. 11 First cracks at 60 kN. The lake blue lines were cracks of horizontal load 60 kN, the blue lines for 70–80 kN, the green lines for 100–140 kN, the yellow lines for 160–180 kN and the pink lines for 200–280 kN

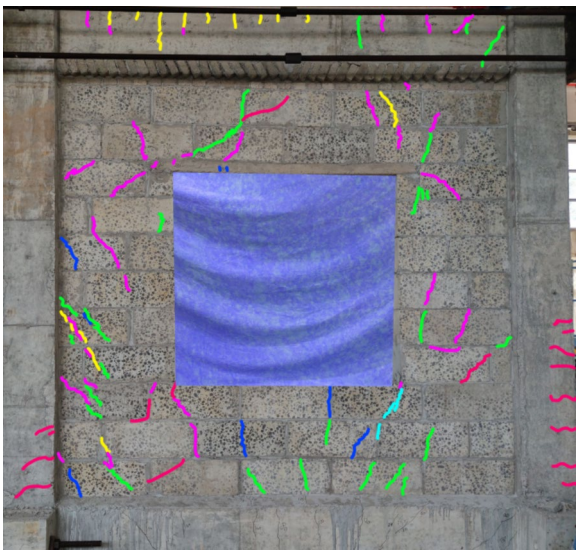

Fig. 12 Cracks distribution at 280 kN. The lake blue lines were cracks of horizontal load 60 kN, the blue lines for 70–80 kN, the green lines for 100–140 kN, the yellow lines for 160–180 kN and the pink lines for 200–280 kN

of approximately 1.5 mm, while other existing cracks exhibited significant increases in width, as shown in Fig. 14 by red lines. During loading, the mortar of the wall exhibited noticeable fragmentation, producing an audible "crack crack" sound. In addition, small cracks appeared at the end of the RC beam and column. In general, the cracks propagated obliquely, with a V-shaped distribution. At the bottom of the infill wall, the cracks were concentrated in the middle, while at the top of the infill wall, the cracks extended into two corners.

Fig. 13 First cracks at 90 kN. The blue lines were cracks of horizontal load at 90 kN, and light green lines at 100–140 kN, and yellow lines at 150–180 kN, and pink lines at 200–250 kN, and red lines at 280 kN

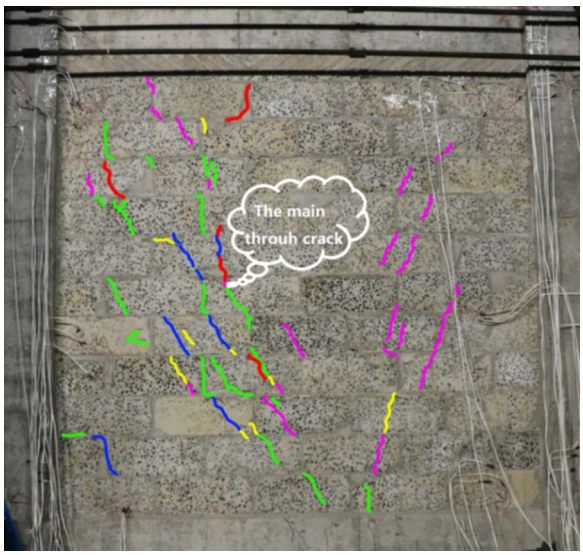

Fig. 14 Cracks distribution at 280 kN. The blue lines were cracks of horizontal load at 90 kN, and light green lines at 100–140 kN, and yellow lines at 150–180 kN, and pink lines at 200–250 kN, and red lines at 280 kN

4 Discussion

4.1 The stiffness change

Based on the horizontal load applied to the frame and the lateral displacement recorded during the test, the lateral stiffness of the tested components can be calculated as K:

$$K = \frac{F}{\Delta} \tag{2}$$

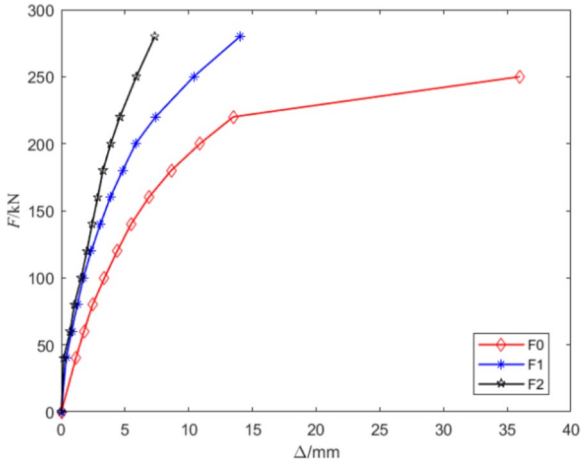

Fig. 15 Relation curve of F–Δ

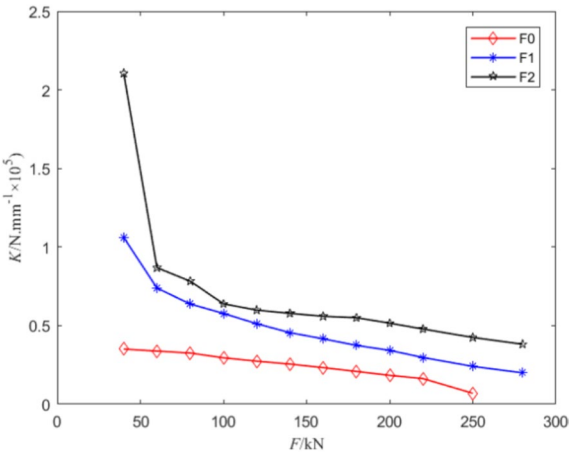

Fig. 16 Relation curve K–F

where F was the horizontal load applied to the axis of the frame beam of the test component, and represented the Δ horizontal drift test value recorded on the axis of the frame beam.

Fig. 15 depicts the correlation between horizontal load F and inter-story drift Δ. As observed from the figure, there was discernible nonlinear correlation between the two parameters, indicating that the lateral stiffness of the specimens was progressively declining with the rise in horizontal loads. Under the same lateral force, the column end displacement of bear frame was the largest, and that of frame with windowless infill wall was the smallest.

The lateral stiffness of the three test specimens decreases with increasing horizontal force, as depicted in Fig. 16. Specifically, when the horizontal load was low (e.g., 40–60 kN), the lateral stiffness test value of the frame with windowless infill wall (F2) decreased rapidly with increasing load, whereas the lateral stiffness of the

bear frame F0 remains nearly constant, and that of the frame with window-infilled wall (F1) lies between the two. Then the frame beam and column were in the elastic stage, and the change in lateral stiffness mainly results from the change in the stiffness of the CACB infill wall in plane. It revealed that small horizontal loads could cause internal damage to the infill wall, even if there were no visible cracks on the wall surface. When the horizontal force was increased to 60–140 kN, the decline rate in measured stiffness of F1 and F2 decreased, and the stiffness contribution of infill wall to the structure declined notably. The decline rate of stiffness of bear frame increased slightly. At 160–250 kN of horizontal force, the stiffness of all three components decreased rapidly, particularly that of F0, which decreased sharply at 220 kN, indicating that the columns and beams of F0 have entered the plastic stage.

The reduction in stiffness ratio of the three test members with respect to their initial stiffness was decrease as the load increased, eventually tending towards consistency when they closed to failure, as demonstrated in Fig. 17. At the beginning of loading, the stiffness ratio of F0 decreased gradually, while that of F1 and F2 declined the most rapidly. During the intermediate stage of loading, the decrease in stiffness ratio of F0 remained approximately constant comparing to beginning, whereas the velocity of decrease in stiffness ratio of F1 and F2 reduced significantly. Towards the later stage of loading, the decrease in stiffness ratio of F0 was markedly accelerated, whereas those of F1 and F2 undergo only slight acceleration. By the end of loading, the lateral stiffness of all three specimens was reduced to roughly 20% of their initial lateral stiffness. Throughout the entire loading process, the stiffness ratio of F0 demonstrated a roughly linear trend with respect to the increase in load, while that of F1 and F2 decreased exponentially. Part of the stiffness of F1 and F2 was provided by infilled walls, and

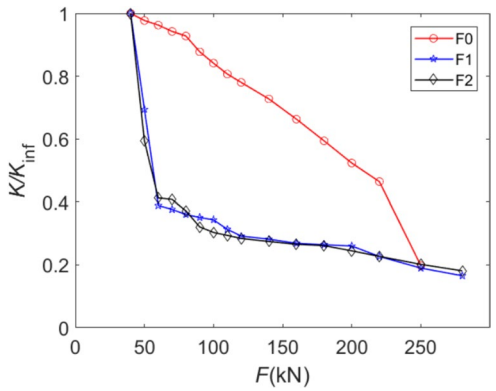

Fig. 17 Variation of stiffness ratio

infilled wall stiffness changes were extremely sensitive to cracking. F0 was a bare frame whose stiffness decreases due to cracks in RC beams and columns. The stiffness of RC beams and columns was not particularly sensitive to crack propagation.

The appearance of cracks in the CACB infill wall was closely linked to the change in the inter-story drift ratio. The first crack in F1 appears at a horizontal load of 60 kN and an inter-story drift ratio of 0.465×10^{-3}. The first crack in F2 appears at a horizontal load of 90 kN and an inter-story drift ratio of 0.426×10^{-3}. It should be noted that infill wall without window could crack at a smaller inter-story drift ratio compared to infill wall with window.

When cracks appear, the inter-story drift of F1 was 1.454 mm, and the measured stiffness decreased to 38.89% of its initial stiffness. In contrast, the inter-story drift of F2 was 1.332 mm, and the stiffness decreased to 32.09% of its initial stiffness. Compared with the initial stiffness, the stiffness of the windowed infill wall frame decreased by 61.11% when cracks appeared, while that of the windowless infill wall frame decreased by 67.91%. This indicates that cracks can cause a decrease in the stiffness of infill frame, and the stiffness of the windowless infill wall frame decreases more than that of the windowed infill wall frame. Figure 18 shows a graph of stiffness degradation with inter-story drift and cracking.

According to the analysis of the experimental results, the main reason for the stiffness change of the experimental models was the softening of the infill wall after cracking. Due to the fact that the concrete beams and columns of the three experimental models were completely identical, and their contributions to the stiffness of the entire model are also the same, the different stiffness changes of the three models can only be caused by changes of the infill walls stiffness. When the inter-story drift ratio was 0.126×10^{-3}, the stiffness of the bare frame decreases by 1.36%, the stiffness of the window filled wall frame decreases by 54.12%, and the stiffness of the windowless filled wall frame decreased by 67.90%. Removing the influence of stiffness changes in reinforced concrete beams and columns, the stiffness of infill walls with windows decreased by 80.22%, while that of infill walls without windows decreased by 81.21%. Therefore, in structural design, the inter-story drift ratio had a significant impact on the stiffness of infill walls; especially the stiffness changes of the overall structure caused by cracking of infill walls cannot be ignored.

4.2 The relation between wall cracking and window opening

It can be seen from the experimental results that the crack load of the infill wall (60 kN) with window was

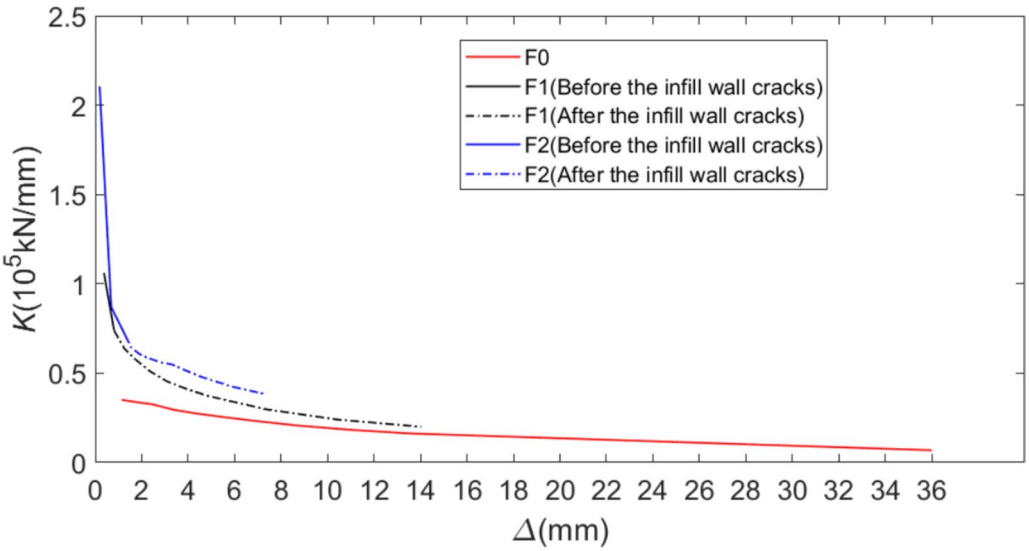

Fig. 18 Stiffness degradation with lateral drift

smaller than that of the non-window infill wall (90 kN), but the inter-story drift ratio of the infill wall with window (θ=1/2149) was larger than that of the non-window infill wall (θ=1/2347). When the wall was cracked, the inter-story drift ratio of the frame was far less than the limit value of the elastic inter-story drift ratio of the frame structure ($[\theta_e]$=1/550) defined by the *Code for Seismic Design of Building* (GB50011-2010, 2010). This indicated that the RC frame was in the elastic stage when the infill wall cracked, whether the infill wall with window or without window in the frame.

According to the test results, the cracking load of the windowless filled frame was 50% greater than that of the windowed filled frame. However, the inter-story drift ratio of cracks in windowless infill walls was slightly lower than that of windowed infill walls. This indicated the horizontal load borne by windowless infill walls was greater than that of windowed infill walls in a building. This means that as the horizontal load and the inter-story drift of buildings increases, the cracking of windowless infill walls will earlier than that of windowed infill wall.

When the inter-story drift ratio of RC frame was close to the limit value of elastic inter-story drift ratio, the horizontal load of windowless filled RC frame was 250–280 kN. In addition, now there were large number of cracks appeared on the wall, and crack width was large. The horizontal load of infilled RC frame with window was 160–180 kN, the cracks on the wall were less and the crack width was smaller.

4.3 Analysis of CACB infill wall cracking in coastal area

The initial cracking of the infill wall was closely related to the inter-story drift ratio of the frame. According to the design and calculation results of a 13-story frame building (Li et al., 2024a) by PKPM software in Taizhou, Zhejiang Province, China, the maximum inter-story drift ratio is shown in Table 6 of bear. The infill wall stiffness was not considered in the frame design by PKPM software, so the calculation results need to be revised according to the test results. Based on the results of this test, when the horizontal force acting on a frame was less than 40 kN, the stiffness of the filled frame with window wall was about 3 times of that to the bare frame, and the stiffness of the filled frame with no-windows wall was about six times of that to the bare frame. It was assumed that 50% of the frames were filled in this 13-story building and the

Table 6 Inter-story drift ratio of the frame ($\times 10^{-3}$)

Stiffness used in the calculation	Seismic intensity of six degree	Wind load of 0.70 kN/m^2	Wind load of 1.0 kN/m^2	Wind load of 1.27 kN/m^2
Bear (Li et a l., 2024a)	0.925	0.925	1.353	1.733
Infill wall without cracks	0.411	0.411	0.601	0.769
Infill wall with cracks	0.601	0.601	0.880	1.127

ratio of infill walls with windows to without windows was 1:5. The total stiffness of this building was 2.250 times to the PKPM calculated value. In design, the inter-story drift ratio was inversely proportional to the stiffness of the structure, so the maximum inter-story drift ratio of the 13-story frame was 44.4% of the calculated value by PKPM. When the infill wall cracked, the stiffness was 1.538 times to the PKPM calculated value. The maximum inter-story drift ratio of the 11-story frame was 65.0% of the calculated value by PKPM. The inter-story drift ratios of the frame calculated by PKPM mode, infill wall without crack stiffness and infill wall with crack stiffness are shown in Table 6.

It could be seen that the maximum inter-story drift ratio was 0.411×10^{-3} (the expression of fractions is: $\theta=1/2433$) under the reference wind pressure by the stiffness of infill wall without crack. According to the test results, when the inter-story drift ratio greater than 0.426×10^{-3}, the infill wall without window will crack, and when the drift ratio was greater than 0.465×10^{-3}, the infill wall with window would crack. This means that when the coastal city encounters a once-in-50-year typhoon, infill wall both with window and without window will not crack.

But the inter-story drift ratio was 0.601×10^{-3} under the wind pressure 1.0 kN/m^2 which calculated by the stiffness of infill wall without cracks. It reached to 0.880×10^{-3} which calculated by the stiffness of infill wall with cracks. All of them were greater than 0.426×10^{-3} (the inter-story drift ratio corresponding to the cracking of infill wall without window) and 0.465×10^{-3} (the inter-story drift ratio corresponding to the cracking of infill wall with window). It means that both infill walls with window and without window cracked.

The inter-story drift ratio was 1.127×10^{-3} under the wind pressure 1.27 kN/m^2 which calculated by the stiffness of infill wall with cracks. This value was much greater than the inter-story drift ratio of cracking, indicating that the infill wall was severely cracked both with window and without window.

The horizontal wind pressure of gusts on the structure will be greater than the reference wind pressure (Li et al., 2024b). The Typhoon Data Records in the local weather station in Lekima landfall 2019 and the reference wind pressure in structure design are shown in Table 7. The peak wind pressure of the gust wind was 1.92 kN/m^2 in Wenling Shitang. The wind pressure based on the 10-min mean maximum wind speed was 1.05 kN/m^2. They were all larger than the reference wind pressure, and lager than the wind pressure 1.0 kN/m^2 too. Even several meteorological stations have gusts wind pressures far exceeding 1.27 kN/m^2. The inter-story drift ratio caused by this wind pressure resulted in severe cracking of the infill wall, according to PKPM calculations and model tests. Therefore, in the coastal areas of Zhejiang province, CACB infill walls with and without windows all will crack under gust wind load.

5 Conclusion

In building design, the function of infill walls is to enclose and separate the building space, without considering its load-bearing capacity, so infill wall cracking does not affect the safety, strength, and stability of the building. It can affect the stiffness of the building, thereby changing the dynamic performance of the building, such as frequency. In addition, it will affect the serviceability of the building and cause it leakage in rainstorm weather. Therefore, sufficient attention needs to be paid to the application research of this type of infill wall. Based on the analysis of the PKPM finite element model and the model test, the conclusions are as follows:

- With the local reference wind pressure, cracks have not appeared in the CACB infill wall of the frame.

Table 7 Wind speed and pressure in Lekima landfall 2019 and the reference wind pressure

No	District	Weather station	Average maximum wind speed of 10 min in Lekima/(m/s)	Maximum wind speed of gusts in Lekima/(m/s)	Wind pressure corresponding to average maximum wind speed of 10 min in Lekima/(kN/m^2)	Wind pressure corresponding to maximum wind speed of gusts in Lekima/(kN/m^2)	Reference wind pressure in structure design/(kN/m^2)
1	Wenling	Shitang	41.1	55.5	1.05	1.92	0.7
2	Wenling	Wenqiao	28.7	51.8	0.51	1.67	0.7
3	Jiaojiang	Taizhouwan bridge	38.4	46.9	0.92	1.37	0.7
4	Wenling	Chengbei	32.0	46.3	0.64	1.34	0.7
5	Wenling	Functional area of grain	28.4	43.2	0.50	1.17	0.7
6	Wenling	Practice base	29.1	43.0	0.53	1.15	0.7

Under the action of gust wind pressure, severe cracking occurred in the CACB infill wall. In addition, when the infill wall creak, the inter-layer drift ratio of reinforced concrete frame is far less than the limit value of the elastic inter-layer drift ratio defined by the *Code for Seismic Design of Building* (GB50011-2010, 2010).

- Under horizontal load, the distribution shape of inclined cracks in two types of infill walls is different. The wall with window cracks beginning from the corners of the window. The distribution shape of the crack is V-shaped below the window hole, and inverted V-shaped above the window hole. The non-window infill wall cracks beginning from the middle of the wall, the distribution shape of the cracks into V-shape.
- The stiffness of infilled frame is much larger than that of bare frame because of the CACB infill wall. Before the infill wall cracks, the stiffness of infilled frame without window is 6 times to that of bare frame, and the stiffness of infilled frame with window is 3 times to that of bare frame. When the infill wall begins cracking, the stiffness of infilled frame without window is 1.926 times to that of bare frame, and the stiffness of infilled frame with window is 1.176 times to that of bare frame. Therefore, the contribution of CACB infill walls to the stiffness of frame structure cannot be neglected in structural design.
- The main reason for the cracking of CACB infill walls in coastal areas Zhejiang province is that the designers did not take reasonable values of wind loads. Compared to the actual wind pressure experienced by the building, the current reference wind pressure value is too small. In building design, it is reasonable to replace the current reference wind pressure with the wind pressure of gusts as the horizontal load.
- The connection method between the infill wall and the frame should be improved, such as leaving gaps between the frame and the infill wall, and using flexible materials to fill them, so that the inter-story drift of the infill wall does not change with the main concrete structure. This requires efforts of engineers and researchers to develop new connection methods in the future. Improving material properties is also an effective method, such as adding fiber materials to CACB to enhance its crack resistance and improve the cracking of infill walls.

Author contributions
Ruige Li: conceptualization, methodology, supervision, project administration, and manuscript drafting. Huadong Cui: calculation, data analysis, statistical interpretation, data visualization, funding acquisition, and formal analysis. Lingchao Ding: data collection, data curation, experimental procedures, and results drafting. Haiping Ni: data collection, interpretation of results, and literature review. Shangquan Xu: experimental procedures and initial manuscript drafting. Huiling Wu: manuscript editing and manuscript revision.

Funding
The authors extend their appreciation to the Department of Science and Technology of Zhejiang Province for funding this work through Zhejiang Provincial Natural Science Foundation Research Project under Grant Number LGG20E080006. The authors extend their appreciation to Zhejiang Mingtou Technology Co., Ltd. for the financial support.

Availability of data and materials
The data sets generated and/or analyzed during the current study are available from the corresponding author at reasonable request.

Declarations

Ethics approval and consent to participate
This study followed ethical standards, and necessary approvals were obtained from the relevant ethics committee. All participants provided informed consent to participate.

Consent for publication
All authors have reviewed and approved the manuscript for publication. Consent was obtained from participants where applicable for publication of data and findings.

Competing interests
The authors declare no competing interests that could have influenced the results or interpretation of this work.

Received: 4 November 2024 Accepted: 14 March 2025
Published online: 11 June 2025

References

Arton, D. D., Qani, K., & Naser, K. (2018). Experimental study on the contribution of masonry infill in the behavior of RC frame under seismic loading. *Engineering Structures, 165*, 27–37. https://doi.org/10.1016/j.engstruct.2018.03.013

Bernhardt, M., Justnes, H., Tellesbo, H., et al. (2014). The effect of additives on the properties of lightweight aggregates produced from clay. *Cement and Concrete Composites, 53*, 233–238. https://doi.org/10.1016/j.cemconcomp.2014.07.005

Chen, Y., Hui, Q. J., & Zhang, H. W. (2020). Experiment and application of ceramsite concrete used to maintain roadway in coal mine. *Measurement and Control, 53*(9–10), 1832–1840. https://doi.org/10.1177/0020294020947134

Cheng, G., Li, Q. H., Su, Z., et al. (2018). Preparation, optimization, and application of sustainable ceramsite substrate from coal fly ash/waterworks sludge/oyster shell for phosphorus immobilization in constructed wetlands. *Journal of Cleaner Production, 175*, 572–581. https://doi.org/10.1016/j.jclepro.2017.12.102

Fan, C. H., Qian, J. S., Yang, Y., et al. (2021). Green ceramsite production via calcination of chromium contaminated soil and the toxic Cr(Vi) immobilization mechanisms. *Journal of Cleaner Production, 315*, 128204. https://doi.org/10.1016/j.jclepro.2021.128204

GB50011–2010. (2010). Code for seismic design of building, Beijing: Ministry of Housing and Urban-Rural Development of the People's Republic of China

Gu, D., Kareem, A., Lu, X., et al. (2023). A computational framework for the simulation of wind effects on buildings in a cityscape. *Journal of Wind Engineering and Industrial Aerodynamics, 234*(1), 105347. https://doi.org/10.1016/j.jweia.2023.105347

Guo, Y., Li, H. Y., & Hu, D. Y. (2011). Performance analysis of aerated ceramsite concrete block. *Create Living, 31*(10), 90–93. https://doi.org/10.3969/j.issn.1003-1324.2011.10.027

He, H. T., Zhao, P., Yue, Q. Y., et al. (2015). A novel polynary fatty acid/sludge ceramsite composite phase change materials and its applications in building energy conservation. *Renewable Energy, 76*, 45–52. https://doi.org/10.1016/j.renene.2014.11.001

Hong L, Cheng W. (2013). Experimental study on high strength composite ceramsite using fly ash and waste glass. *3rd* International Conference on Civil Engineering, Architecture and Building Materials (CEABM 2013) Architecture, building materials and engineering mangment, PTS, 1–4 357–360, pp.1337–1342

Huang, M. F., Li, Q., Chan, C. M., et al. (2024). Performance-based design optimization of tall concrete framed structures subject to wind excitations. *Journal of Wind Engineering and Industrial Aerodynamics, 139*, 70–81. https://doi.org/10.1016/j.jweia.2015.01.005

Huang, M. F., Sun, J. P., Wang, Y. F., et al. (2020). Multi-scale simulation of typhoon wind fields by coupling of weather research and forcasting model and large-eddy simulation. *Jjournal of Wind Engineering and Industrial Aerodynamics, 41*(2), 63–70. https://doi.org/10.1016/j.jweia.2024.105733

Laura, L., Omar, A. S., Claudia, M., et al. (2020). Out-of-plane capacity equations for masonry infill walls accounting for openings and boundary conditions. *Engineering Structures, 207*(15), 110198. https://doi.org/10.1016/j.engstruct.2020.110198

Li, B., & Jiang, L. (2015). *PKPM 2010 structural analysis: From beginner to proficient*. People's Posts and Telecommunications Press.

Li, M., Zhou, D. Y., & Jiang, Y. Q. (2021). Preparation and thermal storage performance of phase change ceramsite sand and thermal storage light-weight concrete. *Renewable Energy, 175*, 143–152. https://doi.org/10.1016/j.renene.2021.05.034

Li, R. G., Gao, Y., Lin, H. J., et al. (2024a). Numerical simulation of infill CACB wall cracking subjected to wind loads. *Structure Engineering and Mechanic, 89*(5), 479–489. https://doi.org/10.12989/sem.2024.89.5.479

Li, R. G., Lin, H. J., Luo, J. D., et al. (2023a). Experimental study on mechanical properties of ceramsite aerated concrete blocks. *China Concrete and Cement Products, 12*, 54–57. https://doi.org/10.19761/j.1000-4637.2023.12.054.04

Li, R. G., Lu, Y. H., Wang, G., et al. (2024b). Experimental study on oblique cracks of ceramsite aerated concrete block-filled walls under typhoon load in coastal area. *Building Structure, 54*(9), 144–149. https://doi.org/10.19701/j.jzjg.20212170

Li, R. G., Luo, J. D., Lu, Y. H., et al. (2022). Experimental study on shrinkage rate of ceramsite aerated concrete. *China Concrete and Cement Products, 10*, 70–73. https://doi.org/10.19761/j.1000-4637.2022.10.070.04

Li, X. L., Zeng, H., Sun, N., et al. (2023b). Preparation of lightweight ceramsite by stone coal leaching slag, feldspar, and pore-forming reagents. *Construction and Building Materials, 370*, 130642. https://doi.org/10.2139/ssrn.4220106

Liu, J. C. (2024). Research on crack resistance of joints in autoclaved ceramic aggregate concrete partition panels. *Engineering and Construction, 38*(2), 368–370. https://doi.org/10.3969/j.issn.1673-5781.2024.02.041

Liu, J. Z., Liu, R., He, Z. M., et al. (2012). Preparation and microstructure of green ceramsite made from sewage sludge. *Journal of Wuhan University of Technology-Materials Science Edition, 27*(1), 149–153. https://doi.org/10.1007/s11595-012-0426-2

Lu, T. S., Liu, S. Y., Cai, G. J., et al. (2021). Study on the disturbance and recompression settlement of soft soil induced by foundation excavation. *Rock and Soil Mechanics*. https://doi.org/10.16285/j.rsm.2020.0980

Lu, X., Lei, J., & Han, M. (2024). Seismic responses and loss evaluation of RC frame with slotted infill walls. *Engineering Structures, 311*, 118214. https://doi.org/10.1016/j.engstruct.2024.118214

Ma, C., Bao, S. X., Zhang, Y. M., et al. (2021a). Preparation of non-sintered sewage sludge based ceramsite by alkali-thermal activation and hydration mechanism. *Ceramics International, 48*(21), 31606–31613. https://doi.org/10.1016/j.ceramint.2022.07.082

Ma, S. C., Gu, Y., & Bao, P. (2021b). Seismic performance of ceramsite concrete T-shaped composite wallboard joints under cyclic loading. *Structures, 33*, 4433–4445. https://doi.org/10.1016/j.istruc.2021.07.023

Ma, S. C., Li, L. H., & Bao, P. (2021c). Seismic performance test of double-row reinforced ceramsite concrete composite wall panels with cores. *Applied Science-Basel, 11*(6), 2688–2688. https://doi.org/10.3390/app11062688

Monical, J., & Pujol, S. (2024). A study of the response of reinforced concrete frames with and without masonry infill walls to earthquake motions. *Structures, 63*, 106345. https://doi.org/10.1016/j.istruc.2024.106345

Ning, N., Ma, Z. J., Zhang, P. P., et al. (2019). Influence of masonry infills on seismic response of RC frames under low frequency cyclic load. *Engineering Structures, 183*, 70–82. https://doi.org/10.1016/j.engstruct.2018.12.083

Niu, X., Huang, W., Zhang, C., et al. (2024). Retrofit of damaged reinforced concrete frame by autoclaved aerated concrete blocks infill wall: Experimental validation and strength estimation. *Journal of Building Engineering, 97*, 110687. https://doi.org/10.1016/j.jobe.2024.110687

Ou, X., & Zhang, W. (2012). *Application of PKPM building structure design program*. Machinery Industry Press.

Pankaj, P., & Ermiao, L. (2005). Material modelling in the seismic response analysis for the design of RC framed structures. *Engineering Structures, 27*(7), 1014–1023. https://doi.org/10.1016/j.engstruct.2005.02.003

Shang, S., Fan, H. H., Li, Y. X., et al. (2022). Preparation of lightweight ceramsite from solid waste using SiC as a foaming agent. *Materials, 15*(1), 325–325. https://doi.org/10.3390/ma15010325

Tan, C. L., Deng, Y., Ren, J., et al. (2018). Study on the mechanical and thermal properties of lightweight and high-strength ceramsite aerated concrete. *New Building Materials*. https://doi.org/10.3969/j.issn.1001-702X.2018.05.028

Wang, J. H., Wang, S. Y., Wang, H., et al. (2022). Influence of ceramsite with assembly unit of sludge and excavated soil on the properties of cement concrete. *Materials, 15*(9), 3164–3164. https://doi.org/10.3390/ma15093164

Wang, N., Liang, L., & Yuan, S. (2013). *Application of PKPM software*. Peking University Press.

Wang, S. (2016). *Detailed explanation of PKPM building structure design examples*. China Electric Power Press.

Wijaya, H., Rajeev, P., Gad, E., et al. (2020). Masonry infill walls significantly contribute to the seismic demand imposed on RC buildings. *Natural Hazards Review*. https://doi.org/10.1061/(ASCE)NH.1527-6996.0000395

Xu, F., Chang, R. C., Zhang, D. L., et al. (2022a). Improvement of CO2-Cured sludge ceramsite on the mechanical performances and corrosion resistance of cement concrete. *Materials, 15*(16), 5758–5758. https://doi.org/10.3390/ma15165758

Xu, F., Liu, W., Bu, S., et al. (2022b). Manufacturing non-sintered ceramsite from incinerated municipal solid waste ash (IMSWA): Production and performance. *Process Safety and Environmental Protection, 163*, 116–130. https://doi.org/10.1016/j.psep.2022.05.007

Xu, R., Zhu, K., Huand, W., et al. (2022c). Experimental study on solidification and road performance of mucky soil. *Journal of Hunan University: Natural Sciences, 49*(3), 167–174. https://doi.org/10.16339/j.cnki.hdxbzkb.2022037

Zhai, H. X., Li, Z., Liao, S. F., et al. (2017). Lightweight self-conserving heat ceramsite autoclaved aerated concrete research. *Journal of Anhui Jianzhu University, 25*(2), 6–10. https://doi.org/10.11921/j.issn.2095-8382.20170202

Zhang, C. Y., Yang, Y. D., Ma, W. K., et al. (2024). Numerical simulation of rupture damage of ceramsite concrete. *Cement, 2024*(3), 7–14. https://doi.org/10.13739/j.cnki.cn11-1899/tq.2024.03.002

Zhang, S. L., Yuan, K., Zhang, J. M., et al. (2020). Experimental study on performance influencing factors and reasonable mixture ratio of desert sand ceramsite lightweight aggregate concrete. *Advances in Civil Engineering, 2020*, 8613932. https://doi.org/10.1155/2020/8613932

Publisher's Note

Springer Nature remains neutral with regard to jurisdictional claims in published maps and institutional affiliations.

Ruige Li, PhD Associate Professor at School of Civil Engineering and Architecture, Taizhou University, China.

Huadong Cui Professor-level Senior Engineer, Director in Charge Taizhou Construction Quality and Safety Service Center, Member of the Construction Quality and Safety Professional Committee, Science and Technology Committee, Zhejiang Provincial Department of Housing and Urban-Rural Development, China.

Lingchao Ding Engineer at Taizhou Yuanxin Construction Engineering Co., Ltd., China.

Haiping Ni Engineer at Taizhou Yuanxin Construction Engineering Co., Ltd., China.

Shangquan Xu Engineer at Taizhou Urban and Rural Planning and Design Institute Co., Ltd., China.

Huiling Wu Engineer at Taizhou Haoqiang Building Materials Co., Ltd, China.